Title

Simulation of plasmonic and photonic crystal structures using Finite-element method

Permalink

https://escholarship.org/uc/item/92b761hs

Author

Yang, Sen

Publication Date

2015

Peer reviewed|Thesis/dissertation

UNIVERSITY OFCALIFORNIA

Los Angeles

Simulation of plasmonic and photonic crystal

structures using finite-element method

A thesis submitted in partial satisfaction of the

requirements for the degree Master of Science in

Material Science and Engineering

by

Sen Yang

2015

ABSTRACT OF THE THESIS

Simulation of plasmonic and photonic crystal structures using Finite-
element method

by

Sen Yang

Master of Science in Material Science and Engineering
University of California, Los Angeles, 2015
Professor Yu Huang, Chair

In this thesis, the Finite-Element Method (FEM) was utilized to simulate and design the optimal nanostructures for better performances of Surface-Enhanced Raman Scattering (SERS) and lasing. FEM proved its effectiveness in the calculations of target physical models to optimize the model geometry or theoretically validate experimental observations.

In chapter 1 and 2, the fundamental theorem of SERS and photonic crystal cavity were introduced and discussed. The most used optical structures for the two effects, metal/dielectric SPP structure and dielectric photonic crystal structure, were introduced as examples. Equations stem from Maxwell equations were derived and discussed to clarify the concepts of SERS and PCC.

In chapter 3, the FEM method was carried out to simulate the SERS performance of Au nano-bowl/SiO_2/Au nanoparticle structure. The electric field distributions and Raman enhancement factors of models in real experiments were calculated and analyzed theoretically. The simulation result on Raman enhancement factors showed consistency with the experimental observations.

In chapter 4, the design process of silicon nitride photonic crystal cavity was introduced and the simulation results were discussed. Using L3 geometrical model, the FEM method successfully revealed the relations between key optical properties, such as quality factor and resonant wavelength, and geometrical parameter selections. The simulations were also helpful in determination of the optimal parameter selection in L3 PCC model for further experimental fabrication.

The thesis of Sen Yang is approved.

Yang Yang

Jaime Marian

Yu Huang, Committee Chair

University of California, Los Angeles

2015

Table of Contents

INTRODUCTION

The design of optical structures for optical enhancement phenomenon, such as Surface-Enhanced Raman Scattering (SERS)[1], stimulated emission[2], enhanced photoluminescence[3], is very important due to their potential applications in photonic devices. Such optical structures include optical micro-cavities[4], metal nanoparticles[5], photonic crystal cavities[6], etc. However, their performances are highly dependent on the geometrical design and model parameter selection, while the analysis of model structure via experiments is both cost and time consuming. To tackle this problem, powerful tools based on computer numerical techniques, such as Finite-Element Method (FEM) and Finite-Different Time-Domain (FDTD), are used to evaluate the performance of target model design.

Surface-enhanced Raman Scattering (SERS), as one of the most spectacular applications of plasmonics, is widely used in chemical detection. It exploits the highly enhanced local electromagnetic field to be coupled with Raman scattering between target molecules and incoming excitation light beam. Early stages of SERS study used roughened metal surfaces[7], from which Raman scattering of single molecules was recorded due to enhanced scattering signal. Further study revealed that highly enhanced local electromagnetic fields due to metal nanoparticle junctions, termed "hot spots", were playing the key role in enabling the amplification of Raman scattering photons by factor up to 10^{14}. To increase the population and intensity of hot spots, many plasmonic nanostructures have been introduced to SERS experiments, such as metal nanoparticles[4, 8] and nanowires [9].

In our study, Au nanobowl/SiO_2/Au nanoparticle platform structure was designed for SERS applications in molecule detection. This structure introduced gold bowl-shaped substrate, silicon dioxide shell and gold nanoparticles distributed on the silicon dioxide shell. The localized surface

plasmon polariton of the gold nanoparticles and the surface plasmon polariton of the gold substrate would couple with each other and produce more hot spots so better SERS performance could be expected. However, the SERS enhancement factors are highly dependent on the parameter selections, such as gold nanoparticle radius, gold nanoparticle density and trigger laser wavelength, while the complexity of the model geometry calls for better design. Using FEM numerical technique, we can improve our model design before experiment and validate our experimental observations.

Optical cavity, as a typical optical structure that can strongly confine light field within a limited volume, has never lost its popularity in many areas of photonic devices. Efforts to optimize optical cavities designs were mainly focused on high quality factor and small modal volume so as to realize strong light-matter interaction.

Photonic crystal is one of the most studied optical structures for waveguides[10] and cavities[6, 11]. Since Eli Yablonovitch and Sajeev John's intensive study on periodic optical structures and its photonic properties such as photonic density of states and photonic band gap[12-15], photonic crystal has appeared in almost all fields of photonic device design, such as LED[16], laser[17], solar cell[18] and optical communication fiber[19]. It has many unique advantages such as high quality factor, small mode value, compatibility with standard CMOS fabrication process, etc.

In this thesis, we also tried to design a silicon nitride photonic crystal cavity for laser design. A frequently used photonic crystal cavity model, L3 model, was taken into account for further optimization. The FEM simulation method was applied on the design process to evaluate the performance of the photonic crystal cavity with different parameter selections and to determine the optimal model parameters. The simulation result provided an optimal design on target model with quality factor of 2563.8.

Chapter I: SURFACE-ENHANCED RAMAN SCATTERING FUNDAMENTALS

A. Surface plasmon polaritons

Surface plasmon polaritons (SPP) are a special electromagnetic phenomenon in which electromagnetic excitations do not propagate in free space but are confined along dielectric and conductor interface and propagate along the surface. Generally speaking, surface plasmon polaritons come from the intercoupling between the electromagnetic fields and oscillating electron plasma inside conductor such as metals and semiconductors.
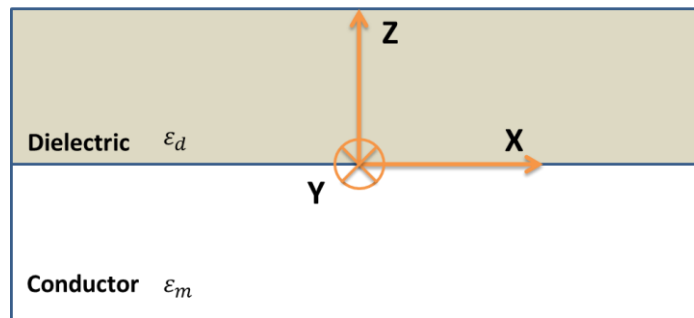

Figure 1-1 Schematic illustration of the dielectric/conductor interfaces and coordinate system. The interface is between dielectric and metal and is infinite in X-Y plane. For Z > 0, the material is dielectrics and the dielectric constant is ε_d. For Z < 0, the material is conductor and the dielectric constant is ε_m.

The nature of surface plasmon polariton can be revealed by Maxwell equations. From the well-known Helmholtz equation and apply it to the dielectric/conductor interface in Fig 1-1:

$$\nabla^2 E + k_0^2 \varepsilon E = 0 \tag{1.1}$$

We can have the wave equation in the form of equation 2.2:

$$\frac{\partial^2}{\partial z^2}\vec{E}(z) + (k_0^2\varepsilon - \beta^2) = 0 \tag{1.2}$$

For harmonic time dependence, we arrive at the following set of coupled equations. For TM modes,

$$E_x = -i\frac{1}{\omega\varepsilon_0\varepsilon}\frac{\partial}{\partial z}H_y \ , \ E_z = -\frac{\beta}{\omega\varepsilon_0\varepsilon}H_y \tag{1.3}$$

For TE modes,

$$H_x = i\frac{1}{\omega\varepsilon_0\varepsilon}\frac{\partial}{\partial z}E_y \ , \ H_z = \frac{\beta}{\omega\varepsilon_0\varepsilon}E_y \tag{1.4}$$

Now, considering that the interface is between conductor and dielectric. Assume that the conductor is metal which has the metallic property that $Re(\varepsilon_m) < 0$.

Then, for TM modes, equation sets 1.3 becomes

$$E_x(z) = A_2 e^{i\beta x}e^{-k_2 z} \ , \ E_z(z) = -A_2\frac{\beta}{\omega\varepsilon_0\varepsilon_m}e^{i\beta x}e^{-k_2 z}, E_x(z) = iA_2\frac{1}{\omega\varepsilon_0\varepsilon_m}k_2 e^{i\beta x}e^{-k_2 z} \tag{1.5}$$

for Z > 0 and

$$H_y(z) = A_1 e^{i\beta x}e^{k_1 z} \ , \ E_x(z) = -iA_1\frac{1}{\omega\varepsilon_0\varepsilon_d}k_1 e^{i\beta x}e^{k_1 z}, E_z(z) = -A_1\frac{\beta}{\omega\varepsilon_0\varepsilon_m}e^{i\beta x}e^{k_1 z} \tag{1.6}$$

for Z < 0.

Then the continuity of E_x and εE_z at the interface requires that $A_1 = A_2$ and $\frac{k_2}{k_1} = -\frac{\varepsilon_m}{\varepsilon_d}$. We also have expressions for k_1 and k_2 that

$$k_1^2 = \beta^2 - k_0^2\varepsilon_d, k_2^2 = \beta^2 - k_0^2\varepsilon_m \tag{1.7}$$

So that the dispersion relation for SPPs at metal/dielectric interface would be

$$\beta = k_0\sqrt{\frac{\varepsilon_m\varepsilon_d}{\varepsilon_m+\varepsilon_d}} \tag{1.8}$$

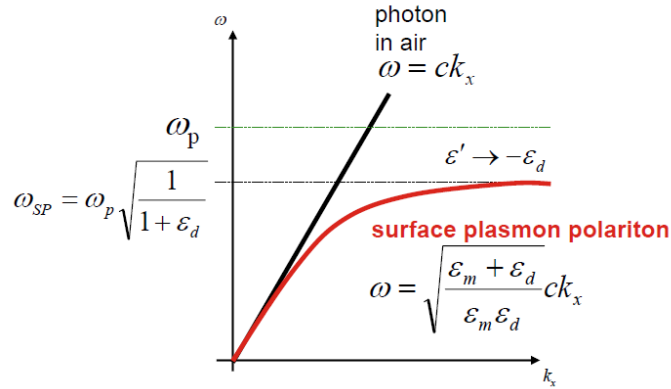And this dispersion relation can be schematically shown in Fig 1-2.

Figure 1-2 The dispersion relation of surface plasmon polariton propagating on dielectric/metal interface. The black line is the dispersion relation of light in air, which the red curve shows the relation of equation 2.8. When $Re(\varepsilon_m) = -\varepsilon_d$, the propagation constant k_x will increase into very big value at the surface plasmon frequency ω_{SP}, just as the equation describes.

B. Localized surface plasmon

In most cases of SERS experiments, structures like metal nanoparticles were used more often than flat dielectric/metal interfaces. This kind of structure leads to the research into localized surface plasmons, in which electromagnetic excitations do not behave as propagating waves but more "localized" oscillations.

We may start from Laplace equation for the electrostatic potential, as shown in equation 1.9:

$$E = -\nabla\Phi \tag{1.9}$$

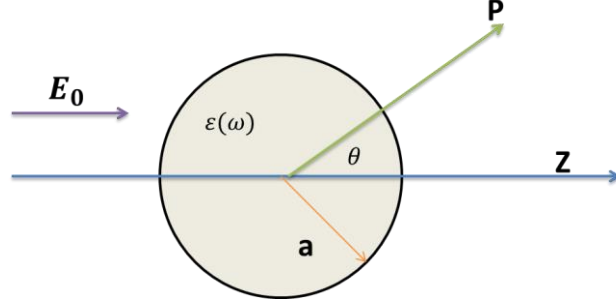And the schematic demonstration of metal nanoparticles is in Fig 1-3.

Figure 1-3. Schematic illustration of a metal nanoparticle in an electrostatic field. The metal nanoparticle has radius a and the electric field direction is aligned with Z direction. The dielectric constant of the metal is denoted as $\varepsilon(\omega)$. The dipole moment $\vec{P}$ is also labeled out to form an angle θ with Z direction.

The general solution is of the form:

$$\Phi(r, \theta) = \sum_{l=0}^{\infty}[A_l r^l + B_l r^{-(l+1)}]P_l(\cos\theta) \tag{1.10}$$

Here $P_l(\cos\theta)$ are the Legendre Polynomials of order l. Apply this equation on the boundary of the particle considering the boundary conditions to solve the potential across the boundary, we have

$$\Phi_{out} = -E_0 r\cos\theta + \frac{\vec{P}\cdot\vec{r}}{4\pi\varepsilon_0\varepsilon_m r^3}, \vec{P} = 4\pi\varepsilon_0\varepsilon_m a^3 \frac{\varepsilon-\varepsilon_m}{\varepsilon+2\varepsilon_m}\vec{E_0} \tag{1.11}$$

As we can see here, the applied field induces a dipole moment inside the sphere. Now we define the polarizability α so that $\vec{P} = \varepsilon_0\varepsilon_m\alpha\vec{E_0}$, then we have experssion for α:

$$\alpha = 4\pi a^3 \frac{\varepsilon-\varepsilon_m}{\varepsilon+2\varepsilon_m} \tag{1.12}$$

So that when $Re(\varepsilon_m) = -2\varepsilon_m$, the localized SPP will be excited and the electromagnetic field will oscillate around the metal nanoparticle surface. This condition is called Frohlich condition[20].

C. Surface-enhanced Raman scattering.

The surface enhanced Raman scattering exploits the highly localized electromagnetic fields around the metal nanostructure to interact with the near-field modes and can greatly enhance Raman scattering of target molecules. The Raman scattering describes the inelastic scattering process between a photon and a molecule, in which the vibration or rotation of the molecule is involved. Therefore, Raman scattering can reveal geometrical feature of target molecule and is usually used as characterization method for chemical analyze.

The vibrational or rotational mode of molecule will lead to the scattering of photon and the incoming photon energy, denoted as $h\upsilon_L$, is shifted in energy by the characteristic energy of vibration $h\upsilon_M$. The corresponding photon energy after Raman scattering will be:

$$\upsilon_S = \upsilon_L - \upsilon_M, \upsilon_{aS} = \upsilon_L + \upsilon_M \tag{1.13}$$

The first is named Stokes scattering and the latter anti-Stokes scattering.

The Raman scattering is a linear process and the power of scattered photon can be analyzed by defining a scattering cross-section σ_R:

$$P_S(\upsilon_S) = N\sigma_R I(\upsilon_L) \tag{1.14}$$

In which N is the population of Raman scattering hot spots and $I(\upsilon_L)$ is the excitation beam intensity.

The enhanced Raman scattering takes effect in two aspects as shown in equation 1.14. At first, the cross section σ_R is increased by adhesion to metal surface. What's more important is that the local electromagnetic field is greatly enhanced due to excitations of localized surface plasmon. A factor named electromagnetic enhancement factor $L(\upsilon) = |E_{loc}(\upsilon)|/|E_0|$ is defined to evaluate the enhancement effect, where $E_{loc}(\upsilon)$ is the local electric field at hot spots. Thus equation 1.14 can be further expressed as

$$P_S(\upsilon_S) = N\sigma_R L(\upsilon_L)^2 L(\upsilon_S)^2 I(\upsilon_L) = RN\sigma_R I(\upsilon_L) \tag{1.15}$$

Where the enhancement of Stokes light beam is

$$R = (\frac{|E_{loc}(v)|}{|E_0|})^4 \qquad (1.16)$$

In other words, the SERS enhancement factor is proportional to the fourth power of the local field enhancement factor.

Chapter II: PHOTONIC CRYSTAL CAVITIES

 A. Introduction to photonic crystal

Photonic crystals are electromagnetic media that usually have a periodic structure consists of materials with different refractive index. The periodic structure of photonic crystals can be seen as an analogue of atomic lattices, in which atoms are organized to form periodic potential barriers for electrons, which lead to electronic band gaps. The different refractive indices of different materials in the media also form a periodic "potential barrier" for electromagnetic waves, thus a "photonic band gap" will exist so that electromagnetic waves in a certain frequency range will not be able to propagate in photonic crystals. The photonic band gap can be derived from Maxwell equations and Bloch theorem, which is similar to the derivation of electronic band gap in solid-state physics.

First we start again from the Maxwell equation:

$$\nabla \cdot \vec{H}(\vec{r},t) = 0 \tag{2.1}$$

$$\nabla \times \vec{E}(\vec{r},t) + \mu_0 \frac{\partial \vec{H}(\vec{r},t)}{\partial t} = 0 \tag{2.2}$$

$$\nabla \cdot \left[\varepsilon(\vec{r})\vec{E}(\vec{r},t)\right] = 0 \tag{2.3}$$

$$\nabla \times \vec{H}(\vec{r},t) - \varepsilon_0 \varepsilon(\vec{r}) \frac{\partial \vec{E}(\vec{r},t)}{\partial t} = 0 \tag{2.4}$$

Assuming that the electromagnetic wave is a plane wave, then we have

$$\nabla \times \vec{E}(\vec{r}) - i\omega\mu_0 \vec{H}(\vec{r}) = 0 \tag{2.5}$$

$$\nabla \times \vec{H}(\vec{r}) + i\omega\varepsilon_0 \varepsilon(\vec{r})\vec{E}(\vec{r}) = 0 \tag{2.6}$$

We can express the equation entirely in $\vec{H}(\vec{r})$, and we get the well-known master equation:

$$\nabla \times \left(\frac{1}{\varepsilon(\vec{r})} \nabla \times \vec{H}(\vec{r})\right) = \left(\frac{\omega}{c}\right)^2 \vec{H}(\vec{r}) \tag{2.7}$$

9

Where $c = \frac{1}{\sqrt{\varepsilon_0 \mu_0}}$.

B. Derivation of photonic band gap

For simplicity, let's assume that the periodicity is in one dimension. The corresponding photonic crystal model is a periodical multilayer film, as shown in Fig 2-1(a). Here we define the "lattice constant" as a, which is the periodicity of the layers in y direction, and the film is infinitely continuous in x and z direction. Then the dielectric constant of this film will also be periodic because of the periodic layers, as shown in Fig 2-1(b). Here we can also use the term "unit cell" in solid-state physics to describe the dielectric constant profile in one period. Then from this periodicity, we have:

$$\varepsilon(\vec{r}) = \varepsilon(\vec{r} + \vec{R}) \tag{2.8}$$

Where $\vec{R} = l\vec{a}$, $l = 0, 1, 2, ...$, and the direction is in y axis.

Consider the modes of the electromagnetic wave and specify the modes by wave vector k_x and k_y. Denote T_R as the translation operator, for the modes of equation (2.7), we have:

$$T_R e^{ik_y(y-la)} = e^{-ik_y la} e^{ik_y y} \tag{2.9}$$

So that we can take linear combination of our modes into the form as:

$$\vec{H}_{k_x,k_y}(\vec{r}) = e^{ik_x x} \sum_m c_m e^{i(k_y + \frac{2\pi}{a}m)y} = e^{ik_x x} e^{ik_y y} \sum_m c_m e^{i\frac{2\pi}{a}my} = e^{ik_x x} e^{ik_y y} u(y) \tag{2.10}$$

Here $u(y)$ is a periodic function in y direction and $u(y + la) = u(y)$. This result is the Bloch's theorem applied on Maxwell equations.
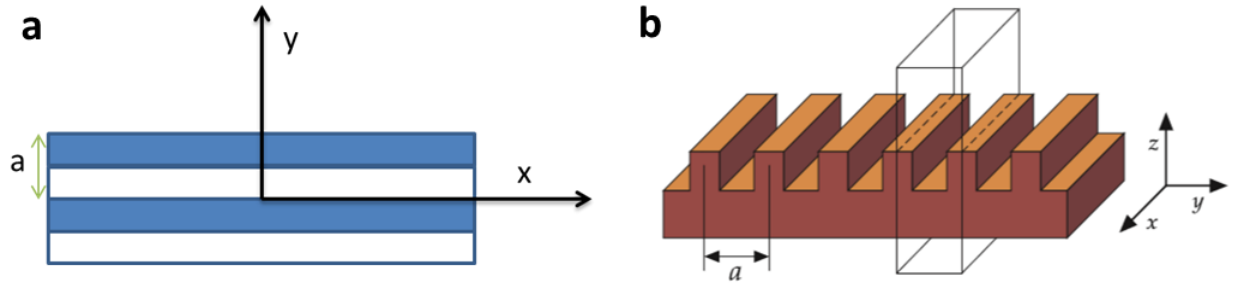
Figure 2-1. Schematic illustration of 1-D photonic crystal structure. (a) The multilayer structure has different materials alternating in Y direction. The periodicity of the alternation is a. The structure is homogeneous in X-Z plane. (b) Periodic dielectric constant profile of the multilayer structure. The alternation of materials in Y direction results in the periodic dielectric constant profile. The dielectric constant profile in one periodicity can be seen as a "unit cell", demonstrated as the box.

Until now we can see that the modes of propagation of electromagnetic wave in periodical dielectric media have the common form with that of electron wave in crystalline lattice. So that at the Brillouin zone boundary, the electromagnetic wave's dispersion relation band diagram will also have a gap so that at certain frequency range, no propagation mode exists. This gap is defined as "photonic band gap".

C. Two-dimensional photonic crystal cavity

If we introduce "defects" into a 2-D array of photonic crystals, light of certain frequency range will be localized around the defect point, and in fact this structure can behave as a cavity to confine the light in a certain region.

Until now many geometrical models of 2-D photonic crystal cavity have been introduced for applications of photonic devices, such as laser and LED and were widely used in the study of

photonics like spontaneous emission control. These models differ in the way they introduce defects.

One of the most used 2-D photonic crystal cavity model is the L3 model[11]. This structure is formed by a line of three missing holes in a triangular lattice pattern of air holes and the air holes at the cavity edge shifted, as shown in Fig 2-2(a). Line defect can also induce localized photonic states around defect region to behave as a photonic cavity[6], as shown in Fig 2-2(b). The middle line of air holes were removed to form a line defect while the lattice constants of the three lateral regions were different, which formed a "photon potential well" in the middle region.
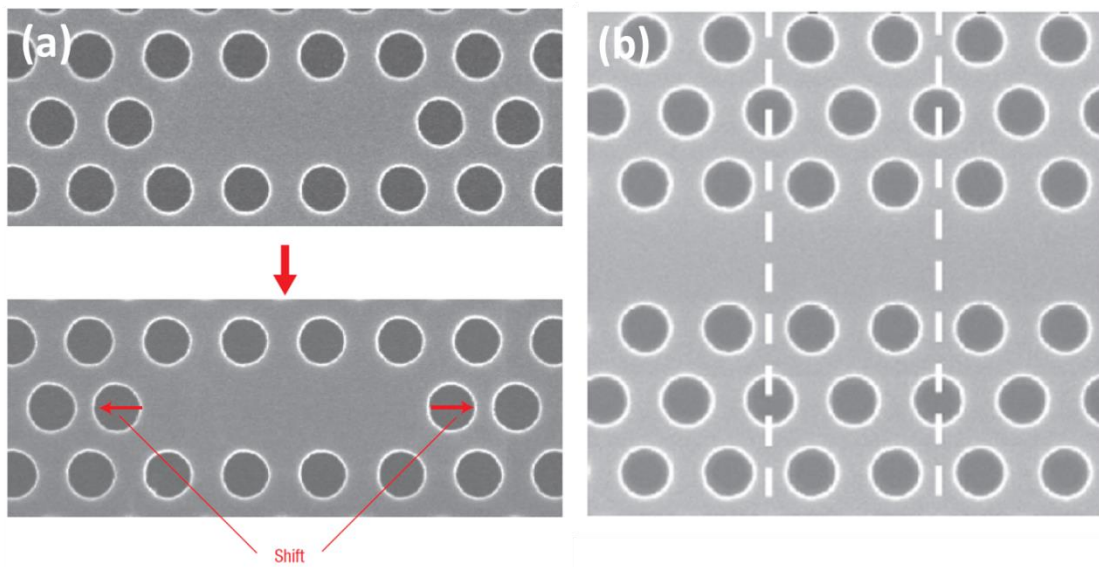

Figure 2-2. Schematic illustration of photonic crystal cavity models. (a) Schematic view showing the L3 photonic crystal cavity model. The left and right air holes at cavity boundaries were shifted outward to improve the quality factor. Reproduced from Ref. 11. (b) Schematic view of line defect photonic crystal cavity model. Reproduced from Ref. 6.

Chapter III: SIMULATION OF PARTICLE-DRESSED, SILICA SHELL-ISOLATED CAVITY ARCHITECTURE FOR SURFACE-ENHANCED RAMAN SCATTERING

A. Simulation of Electric field amplitude

In this project, the simulation was carried out using FEM method to calculate the electric field distribution and SERS enhancement factors of the models in real experiments. Three models were constructed and simulated: gold nano-bowl array without gold nanoparticles; gold nano-bowl array with gold nanoparticles of radius = 16 nm; gold nano-bowl array with gold nanoparticles of radius = 30 nm.

To construct the model geometry, Matlab was used to calculate the population and positions of nanoparticles according to experimental setup parameters, as shown in Appendix I. The radius of the gold nano-bowl and the average distance between nanoparticles in real samples were measured from SEM images and the thickness of silica from ellipsometer. Assuming that the nanoparticles were evenly distributed along the silica surface, the Conjugate Gradient Method was used to calculate the position of each particle that can be grown onto the substrate.

In the simulation, the input excitation light beam's electric field was set as 1V/m and its wavelength is 632.8 nm. The gold bowl radius R was 310 nm and height H was 496 nm. The silica thickness h was 7.276 nm. The gold nanoparticle radius r was 16nm or 30nm, depending on simulation models. The model is shown in Fig 3-1. The electric field distributions of designed models are shown in Fig 3-2.
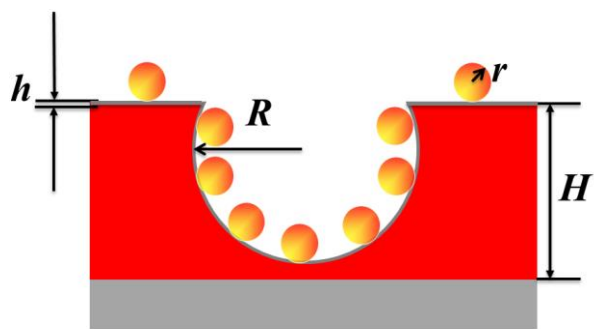
Figure 3-1. Schematic illustration of Au nano-bowl/SiO₂/Au nanoparticle model. A layer of gold nano-bowl structure was fabricated onto SiO_2 substrate, coated by a layer of silica. Gold nanoparticles were dressed onto the surface of silica coating layer. Parameters: h, thickness of silica coating layer. R, radius of gold nano-bowl structure. R, thickness of gold layer. r, radius of gold nanoparticle. Reproduced from Ref. 21.

The electric field distributions in three models revealed the significance of gold nanoparticles in electric field enhancement. The electric field pattern in Fig 3-2(a), when no gold nanoparticle was dressed on silica surface, has strong electric field amplitude in air and Au/SiO₂ bowl corner instead of the inner surface of the bowl, indicating weak SERS enhancement factors because most molecules would be distributed on the bowl inner surface. When gold nanoparticles with radius = 16 nm were dressed onto the inner surface of Au/SiO₂ bowl, the electric field along the Au/SiO₂ bowl inner surface was stronger than that in Fig 3-2(a). In Fig 3-2(c), electric field along the Au/SiO₂ bowl inner surface was further enhanced, indicating better SERS enhancement than in Fig 3-2(b).
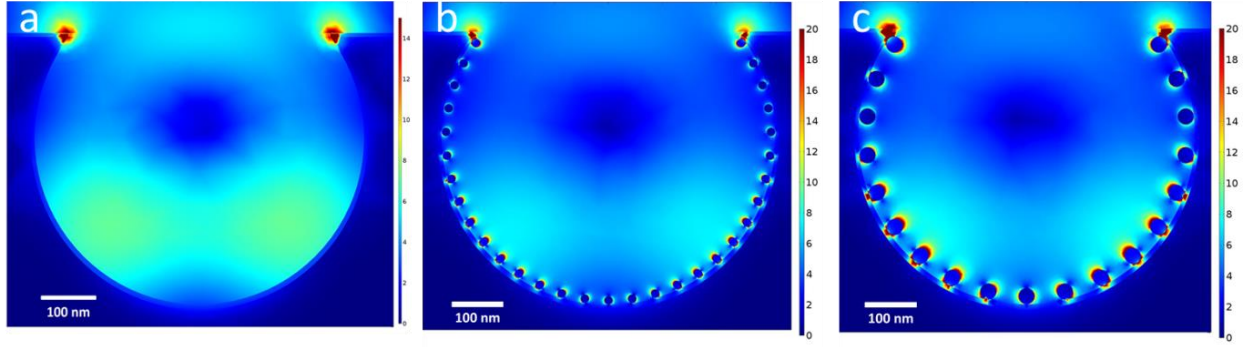
Figure 3-2. The electric field amplitude of Au nano-bowl/SiO₂/Au nanoparticle models.

(a) Au nano-bowl/SiO$_2$/Au nanoparticle model without gold nanoparticles. (b) Au nano-bowl/SiO$_2$/Au nanoparticle structure with gold nanoparticle radius = 16 nm. (c) Au nano-bowl/SiO$_2$/Au nanoparticle structure with gold nanoparticle radius = 30 nm. Reproduced from Ref. 21.

B. Simulation of Raman enhancement factor

SERS is mainly contributed by hot spots around which the electric field is enhanced to be extremely strong. From the theoretical discussion in chapter 1, the maximum enhancement factor predicted is proportional to E^4, where $E = E_{loc}/E_{in}$, E_{loc} and E_{in} are the electric field amplitude at the hot spot and incoming port, respectively. Thus from the calculated electric field distribution, we can anticipate the possible maximum Raman enhancement factor along Au/SiO$_2$ bowl inner surface in different models.

From the electric field amplitude results, the value of E_{loc}/E_{in} of the model with 16 nm gold nanoparticle was 19.5, and the model with 30 nm gold nanoparticle had the E_{loc}/E_{in} value of 25.4. The Raman enhancement factors calculated from electric field amplitudes were 1.446×10^5 for the model with 16 nm gold nanoparticles and 4.162×10^5 for the model with 30 nm gold

nanoparticles, respectively.

C. Experimental setup

The designed Au nano-bowl/SiO$_2$/Au nanoparticle models were fabricated after simulation, followed by SERS experiments to evaluate the real SERS performance of the designed structure. Pyridine was used as the probe molecule to demonstrate SERS behaviors and its predominate peaks are at 1013 and 1038 cm^{-1}. To better demonstrate the SERS effect of designed models, gold nanoparticles with radius of 16 nm and 30 nm were coated on silica flat substrates for better comparison.

The fabrication process is shown in Fig 3-3[21]. Briefly, monolayer colloidal crystal template of 620 nm polystyrene (PS) spheres were self-assembled at a water-air interface. The template was transferred onto gold-coated glass slide. Then gold was electrodeposited through the template. The height of gold deposition was controlled to be 496 nm. After removal of the PS spheres, a layer of SiO$_2$ was grown on gold nano-bowl structure via surface sol-gel method. Then gold nanoparticles with radius 16 nm or 30 nm were anchored by a layer of (3-aminopropyl)trimethoxysilane (APTS) coated on SiO$_2$ surface and were immobilized in the cavity by immersing in gold nanoparticle colloids.
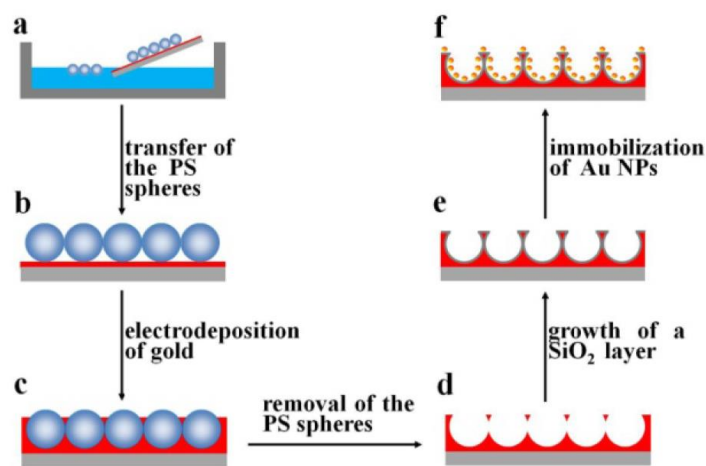
Figure 3-3. Schematic diagram of the preparation procedures for the Au nano-bowl/SiO₂/Au nanoparticle structure. (a) Self-assembly of monolayer template of 620nm PS spheres at water-air interface. (b) Transfer of the template onto gold-coated glass slide. (c) Electrodeposition of gold. (d) Removal of the PS spheres. (e) Surface sol-gel growth of ultrathin silica shell. (f) Immobilization of gold nanoparticles. Reproduced from Ref. 21.

D. Experimental results

As shown in Fig 3-4 and Fig 3-5, the experiment results agreed well with simulation results[21]. Fig. 3-4 showed the SEM images of gold nanoparticles with radius of 16nm and 30nm dressed on gold nano-bowl/silica substrates and flat silica substrates. Fig 3-5 showed the Raman spectra of pyridine molecules on the four different substrates.
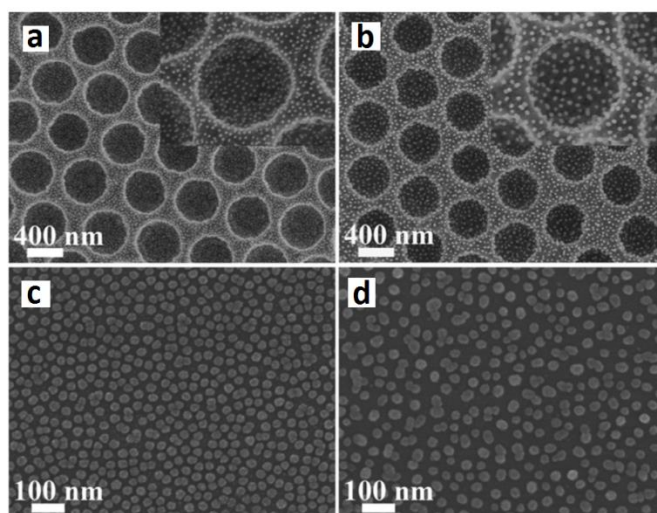
Figure 3-4. SEM images of experiment samples. (a) Au nano-bowl/SiO$_2$/Au nanoparticle structure with 16 nm gold nanoparticle. (b) Au nano-bowl/SiO$_2$/Au nanoparticle structure with 30 nm gold nanoparticle. (c) 16 nm gold nanoparticle coated on flat silica substrate. (d) 30 nm gold nanoparticle coated on flat silica substrate. Reproduced from Ref. 21.
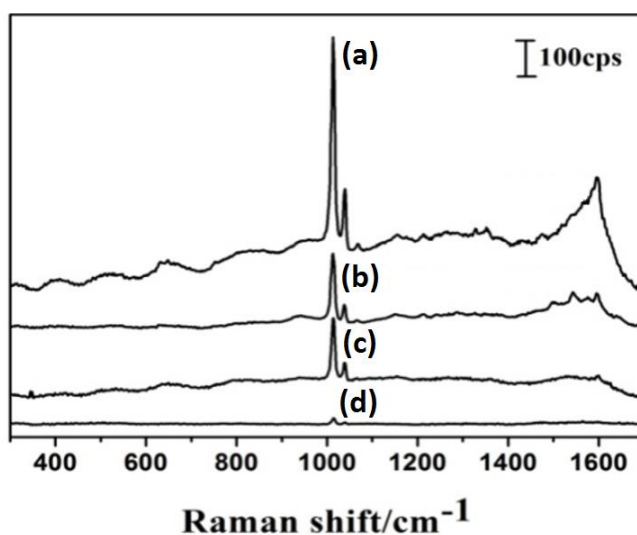

Figure 3-5. SERS spectra of 1mM pyridine solution on different substrates. (a) Au nano-bowl/SiO$_2$/Au nanoparticle structure with 30 nm gold nanoparticle. (b) 30 nm gold nanoparticle coated on flat silica substrate. (c) Au nano-bowl/SiO$_2$/Au nanoparticle structure with 16 nm gold nanoparticle. (d) 16 nm gold nanoparticle coated on flat silica substrate. Reproduced from Ref. 21.

First the effectiveness of gold nano-bowl structure is proved to be significant. The intensity of characteristic peak of pyridine on Au nano-bowl/SiO_2/Au nanoparticle substrate is 5 times of that on flat silica substrate. This is contributed by the strong particle-cavity coupling between gold nanoparticle and gold nano-bowl substrate. Second, the peak intensity is higher when the nanoparticle radius is 30nm. The ratio of peak intensities of pyridine on Au nano-bowl/silica/Au NP substrate with particle radius of 30nm and 16nm is around 3, which agrees well with the value of 2.8 from simulation results.

E. Summary

In this project, FEM method was carried out to simulate the Raman enhancement factors of the physical models we used in experiments. The simulation and experiment results all revealed the effectiveness of Au nano-bowl/silica/Au nanoparticle structure in SERS applications. The simulation also anticipated that the Au nano-bowl/silica/Au nanoparticle structure with 30 nm gold nanoparticles will have better SERS performance than the model with 16 nm gold nanoparticles, which is consistent with experimental observations. What's more, the simulation results anticipated that the Raman enhancement factor of the model with 30 nm gold nanoparticles would be about 2.8 times of the Raman enhancement factor of the model with 16 nm gold nanoparticles, which agreed well with experimental observations.

Chapter IV: DESIGN OF SILICON NITRIDE PHOTONIC CRYSTAL CAVITY

A. Goal of design

In recent years, perovskite has been attracting the attention of research groups worldwide because of its unique photonic properties. Many photonic devices such as solar cell[22-23], LED[24] and photodetector[25] have been realized using perovskite. However, successful reports of perovskite laser are much fewer.

The primary difficulty of perovskite laser is to design an optical cavity that has high quality factor and should be coupled well with perovskite. In this chapter, the Finite-element Method was used to numerically simulate a L3 photonic crystal cavity[26] for optimal parameter set. To design an ideal photonic crystal cavity for perovskite laser, we need to consider two variables: the resonant wavelength of fundamental cavity mode and the quality factor. The resonant wavelength of fundamental cavity mode should be as close to the photoluminescence peak of perovskite as possible so that the perovskite could be coupled to the cavity. The quality factor, on the other hand, is used to evaluate the ability of the cavity to confine photons inside the cavity. Higher quality factor means lower lasing threshold thus it would be easier to achieve stimulated emission effect on perovskite.

In our simulation, we first constructed L3 photonic crystal cavity design that has the resonant wavelength of fundamental cavity mode in the range of 750 nm to 760 nm. Then we tried different parameter sets in simulation and select the parameter sets with highest quality factor as the optimal design.

B. Physical model design

The material chosen for the photonic crystal cavity is important. Most reports about photonic crystal cavities made use of material systems with high refractive indices, such as Si^{27} or $InAs^{28}$. Generally, high refractive index would make it easier to achieve high quality factor due to higher

reflectivity, however the resonant wavelengths of photonic crystal cavities made of high refractive index materials were usually in the near infrared spectral region, thus they were not ideal candidates for our design. To tune the resonant wavelength around the wavelength region of our goal while still maintain a relatively large quality factor, we need to choose our candidate material from other material systems to extend the resonant wavelength into the visible range yet still maintain sufficient quality factor.

Nitride materials are possible candidates. Former reports of photonic crystal cavities made of nitride materials such as AlN[29] and GaN[30] showed resonant wavelengths in visible region. However, III/V semiconductor photonic crystal structure is hard to process, especially the fabrication of free-standing slab structure. Thus we choose Si_3N_4, which has a refractive index of 1.99, as our material. It is fully compatible with standard CMOS fabrication process and is very cost-effective.

In this project, the L3 photonic crystal cavity is used. The L3 cavity introduces point defect around the cavity region, which consists of three missing air holes in a row. The air holes at the cavity left and right boundaries were shifted outward by a distance d, and they both have radius r_1. It supports a spectrally well separated fundamental mode with small mode volume and can be optimized to have high quality factors by adjusting the size and position of surrounding air holes in the cavity. The two-dimensional demonstration of L3 model is shown in Fig. 4-1(a).
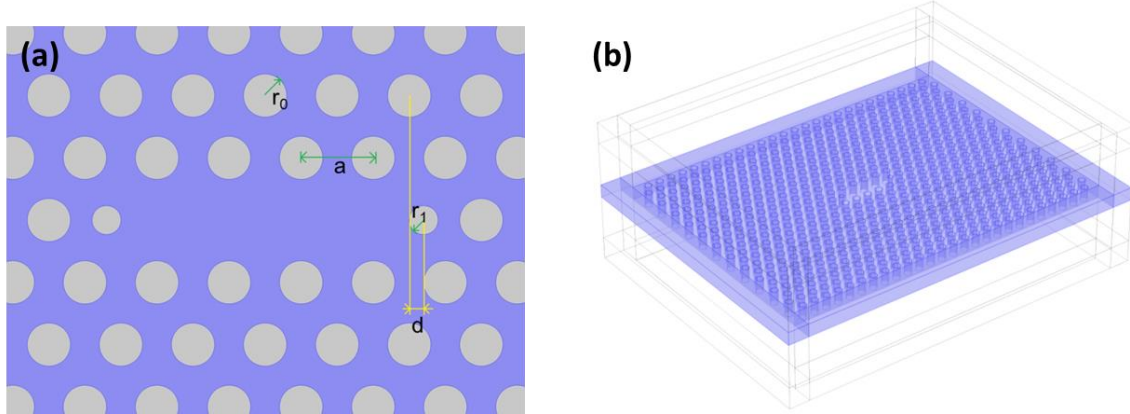
Figure 4-1. Schematic representation of the L3 photonic crystal cavity geometry.

Parameters in (a): r_0, the radius of normal air holes. a, the lattice constant. r_1, the radius of air holes at the left and right boundary of the cavity region. d, the shift of air holes at left and right cavity boundaries. (b) Three-dimensional view of the model structure. The photonic crystal cavity slab is suspended on air layer for better quality factor.

The Si_3N_4/air photonic crystal cavity is a free-standing slab suspended on air. The three-dimensional model is shown in Fig 4-1(b). This model includes 23 periods in row and 27 periods in column, in which the air holes are organized to form a triangular lattice. The reason to include so many periods in our design is that we need better light confinement in lateral direction for this relatively low refractive index system. The lattice constant was chosen to be 300 nm and the radius of air holes was chosen as 90 nm so that the wavelength requirement will be fulfilled. The thickness of the slab was chosen to be one lattice constant a. Then we adjusted the parameter set of r_1 and d to optimize our design.

The simulation results were based on the following parameter sets: r_1/a = 0.1, 0.15, 0.2, 0.25, and d/a = 0.1, 0.15, 0.2, 0.25. At first glance the electric field pattern of the cavity fundamental

mode was analyzed. Then the energy density spectrums of different models with different parameter sets were calculated and discussed. After the energy density spectra, cavity fundamental mode wavelengths and quality factors were compared among all parameter selection sets. The parameter set with highest quality factor was chosen as the final result.

C. Simulation of cavity fundamental mode electric field pattern

In the parameter selections, two parameters were chosen as the key variables in optimization of the cavity performance. They were r_1(the radius of air holes at the left and right boundary of the cavity region) and d(the displacement of left and right boundary air holes). The electric field patterns were organized to show the effect of changing these two variables.

The electric field patterns of fundamental mode in our models in different parameter selection sets were shown in Fig 4-2 to Fig 4-17. For all models, the radius of normal air hole was 90 nm and lattice constant was 300 nm.
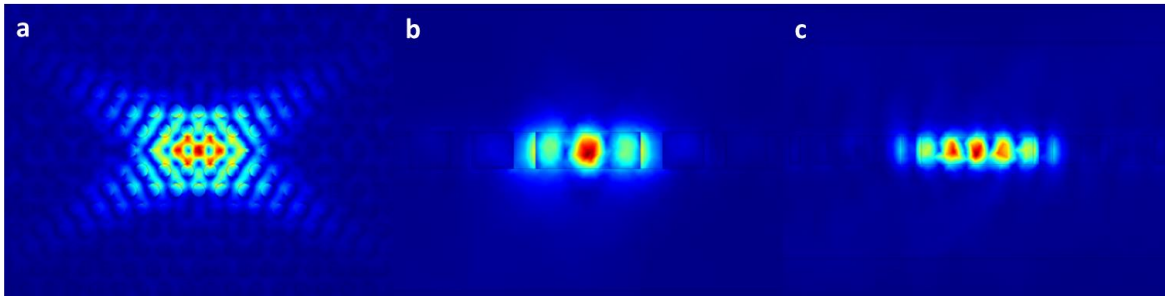

Figure 4-2. Electric field pattern of cavity fundamental mode with $\frac{r_1}{a} = 0.1, \frac{d}{a} = 0.1$**.** (a) Electric field pattern in X-Y plane. (b) Electric field pattern in Y-Z plane. (c) Electric field pattern in X-Z plane.
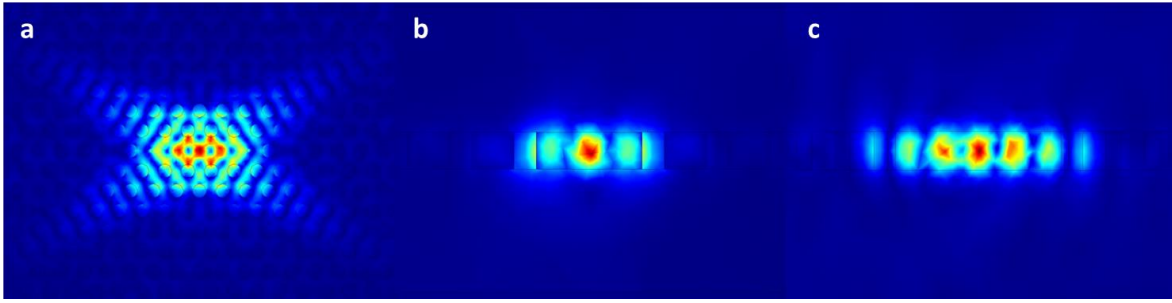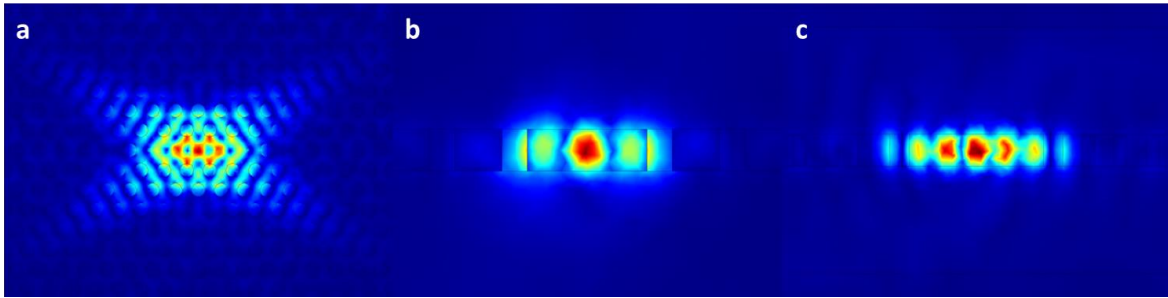
Figure 4-3. Electric field pattern of cavity fundamental mode with $\frac{r_1}{a} = 0.1, \frac{d}{a} = 0.15$**.** (a) Electric field pattern in X-Y plane. (b) Electric field pattern in Y-Z plane. (c) Electric field pattern in X-Z plane.
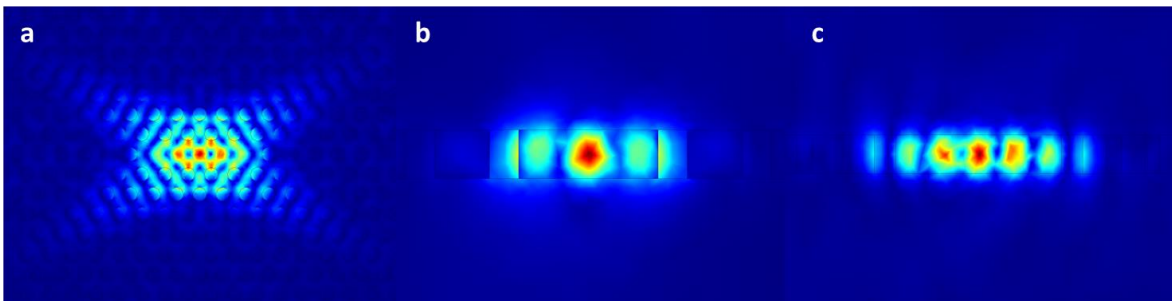

Figure 4-4. Electric field pattern of cavity fundamental mode with $\frac{r_1}{a} = 0.1, \frac{d}{a} = 0.2$**.** (a) Electric field pattern in X-Y plane. (b) Electric field pattern in Y-Z plane. (c) Electric field pattern inX-Z plane.

Figure 4-5. Electric field pattern of cavity fundamental mode with $\frac{r_1}{a} = 0.1, \frac{d}{a} = 0.25$**.** (a) Electric field pattern in X-Y plane. (b) Electric field pattern in Y-Z plane. (c) Electric field pattern in X-Z plane.
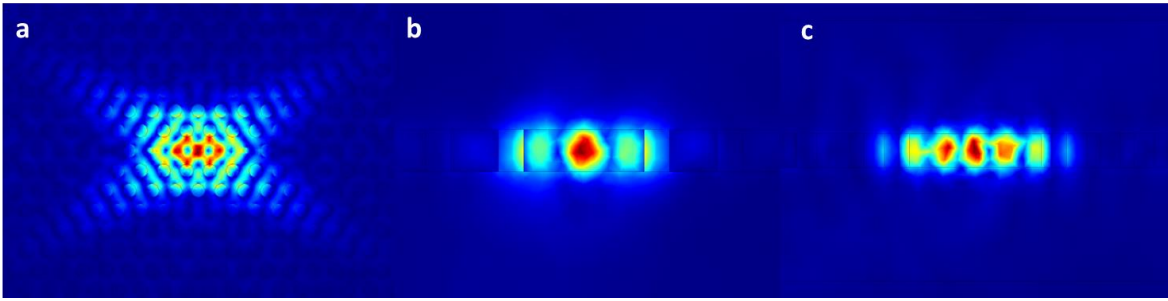
Figure 4-6. Electric field pattern of cavity fundamental mode with $\frac{r_1}{a} = 0.15, \frac{d}{a} = 0.1$. (a) Electric field pattern in X-Y plane. (b) Electric field pattern in Y-Z plane. (c) Electric field pattern in X-Z plane.
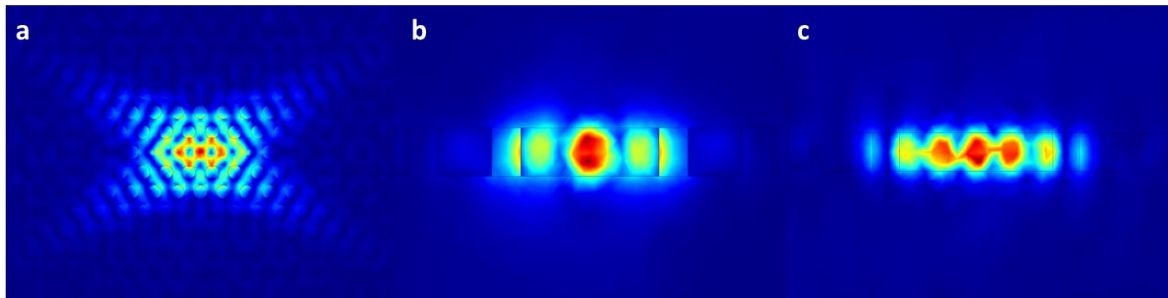

Figure 4-7. Electric field pattern of cavity fundamental mode with $\frac{r_1}{a} = 0.15, \frac{d}{a} = 0.15$. (a) Electric field pattern in X-Y plane. (b) Electric field pattern in Y-Z plane. (c) Electric field pattern in X-Z plane.

Figure 4-8. Electric field pattern of cavity fundamental mode with $\frac{r_1}{a} = 0.15, \frac{d}{a} = 0.2$. (a) Electric field pattern in X-Y plane. (b) Electric field pattern in Y-Z plane. (c) Electric field pattern in X-Z plane.
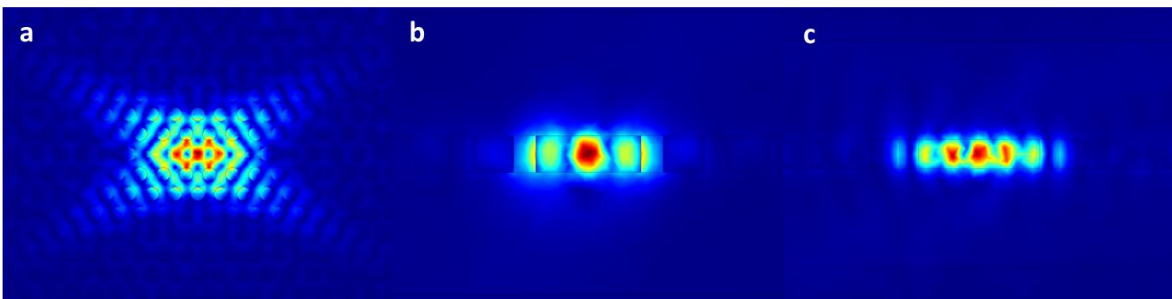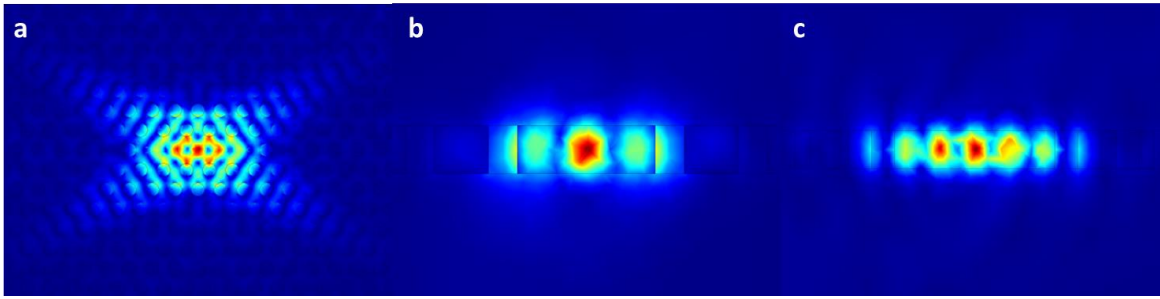
Figure 4-9. Electric field pattern of cavity fundamental mode with $\frac{r_1}{a} = 0.15, \frac{d}{a} = 0.25$**.** (a) Electric field pattern in X-Y plane. (b) Electric field pattern in Y-Z plane. (c) Electric field pattern in X-Z plane.

Figure 4-10. Electric field pattern of cavity fundamental mode with $\frac{r_1}{a} = 0.2, \frac{d}{a} = 0.1$**.** (a) Electric field pattern in X-Y plane. (b) Electric field pattern in Y-Z plane. (c) Electric field pattern in X-Z plane.

Figure 4-11. Electric field pattern of cavity fundamental mode with $\frac{r_1}{a} = 0.2, \frac{d}{a} = 0.15$**.** (a) Electric field pattern in X-Y plane. (b) Electric field pattern in Y-Z plane. (c) Electric field pattern in X-Z plane.
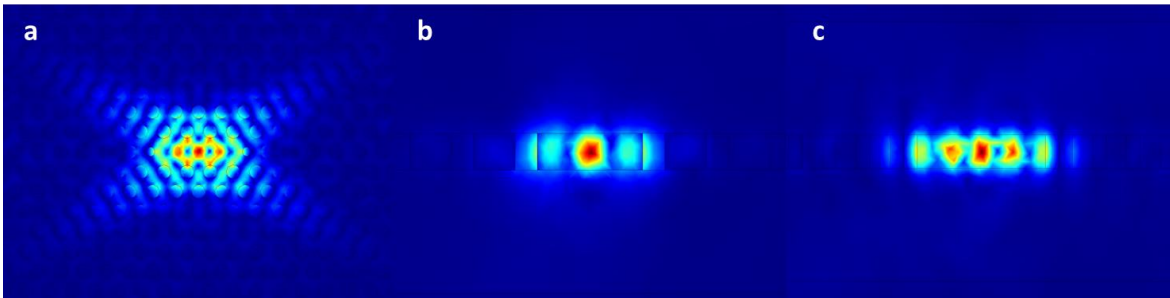
Figure 4-12. Electric field pattern of cavity fundamental mode with $\frac{r_1}{a} = 0.2, \frac{d}{a} = 0.2$**.** (a) Electric field pattern in X-Y plane. (b) Electric field pattern in Y-Z plane. (c) Electric field pattern in X-Z plane.

Figure 4-13. Electric field pattern of cavity fundamental mode with $\frac{r_1}{a} = 0.2, \frac{d}{a} = 0.25$**.** (a) Electric field pattern in X-Y plane. (b) Electric field pattern in Y-Z plane. (c) Electric field pattern in X-Z plane.
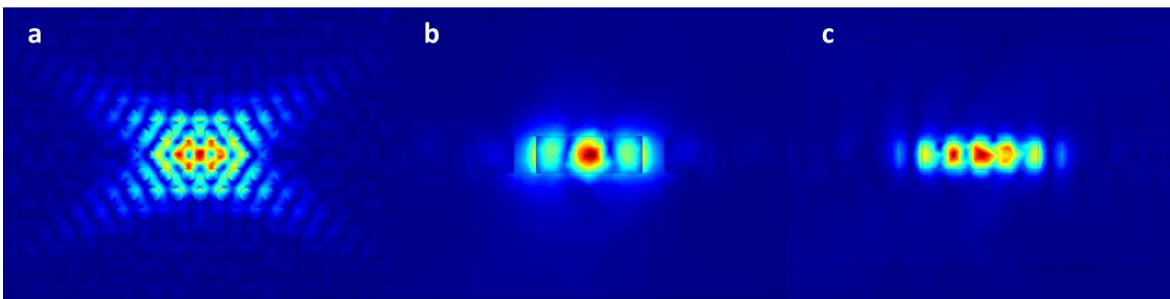

Figure 4-14. Electric field pattern of cavity fundamental mode with $\frac{r_1}{a} = 0.25, \frac{d}{a} = 0.1$**.** (a) Electric field pattern in X-Y plane. (b) Electric field pattern in Y-Z plane. (c) Electric field pattern in
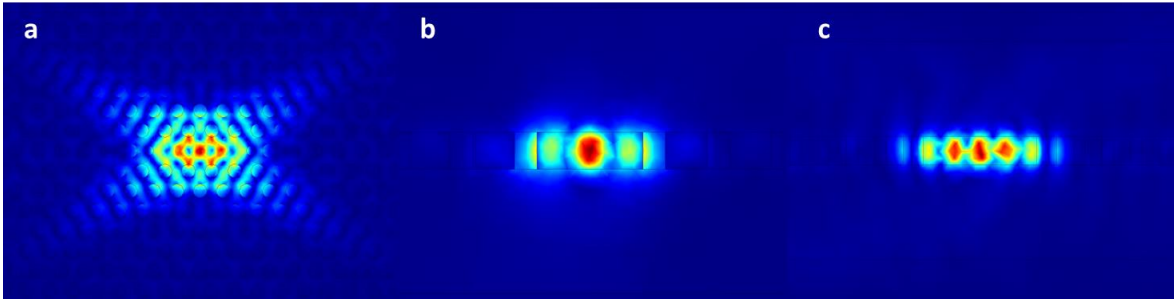
X-Z plane.

Figure 4-15. Electric field pattern of cavity fundamental mode with $\frac{r_1}{a} = 0.25, \frac{d}{a} = 0.15$. (a) Electric field pattern in X-Y plane. (b) Electric field pattern in Y-Z plane. (c) Electric field pattern in X-Z plane.

Figure 4-16. Electric field pattern of cavity fundamental mode with $\frac{r_1}{a} = 0.25, \frac{d}{a} = 0.2$. (a) Electric field pattern in X-Y plane. (b) Electric field pattern in Y-Z plane. (c) Electric field pattern in X-Z plane.
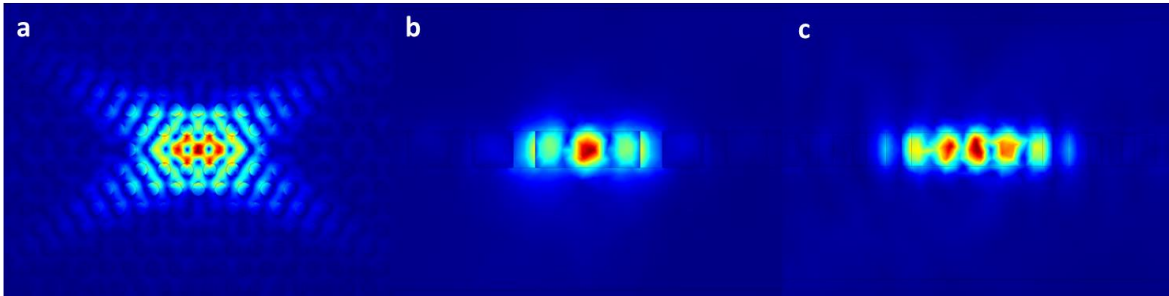

Figure 4-17. Electric field pattern of cavity fundamental mode with $\frac{r_1}{a} = 0.25, \frac{d}{a} = 0.25$. (a) Electric field pattern in X-Y plane. (b) Electric field pattern in Y-Z plane. (c) Electric field pattern in
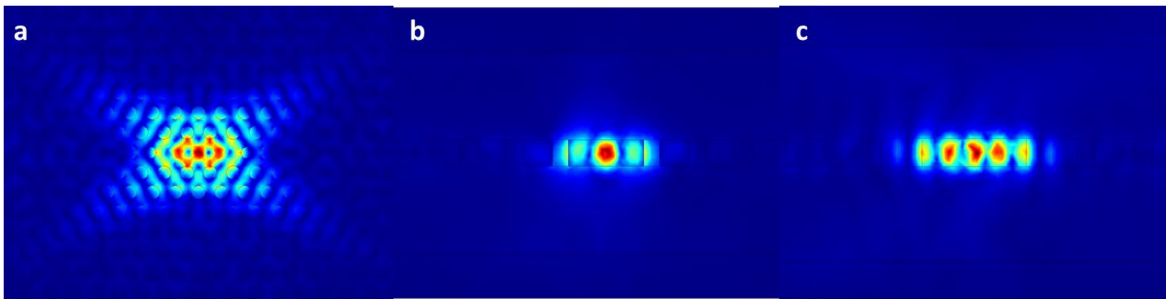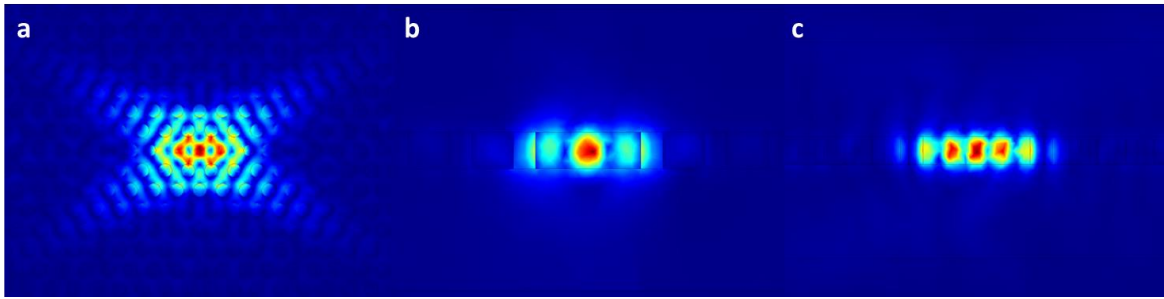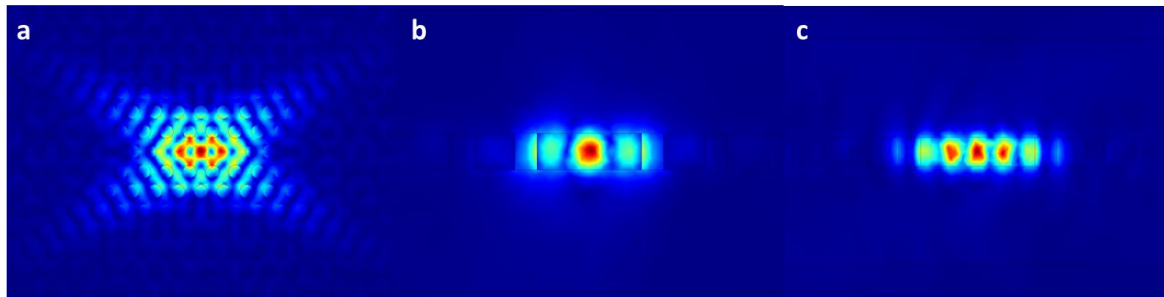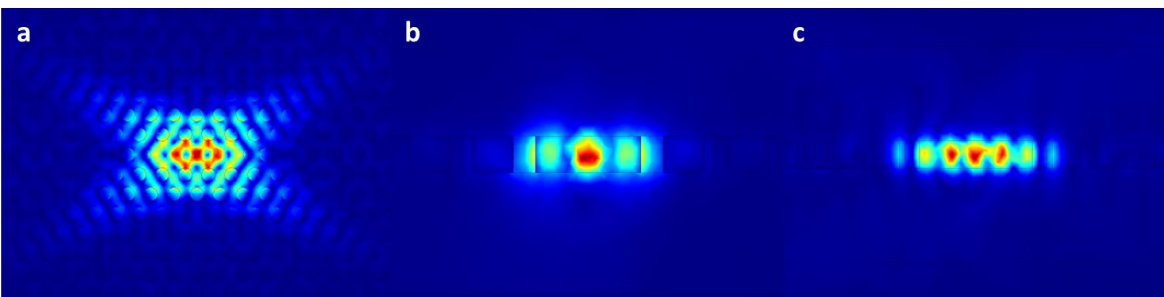
X-Z plane.

The X-Y view of electric field patterns in all models were typical pattern of cavity fundamental mode of L3 cavity model. The electric field was strongest at the three point defect positions. Generally the effectiveness of the cavity to confine light can be evaluated by looking at the electric field amplitude outside the cavity region: cavity with weaker electric field outside cavity region has higher quality factor.

The Y-Z views of electric field pattern showed light confinement in Y direction and Z direction. They clearly demonstrated that current mode is the fundamental mode in Y direction: only one electric field maxima showed up in the cavity region in Y direction. The electric field distribution in Z direction showed that the electric field amplitude in air is much smaller than that in silicon nitride.

The X-Z views of electric field pattern showed the three electric field maxima in cavity region. It also demonstrated the effectiveness of the cavity in confining light in X direction: the electric field reduced rapidly across the boundary air holes.

D. Simulation of cavity energy density spectrum

From the electric field pattern, we can roughly evaluate the performance of the cavity models by estimate the electric field amplitude inside and outside the cavity region. However, to evaluate the effectiveness of the cavity models in confining light quantitatively, we need to numerically calculate the energy density spectrum in cavity region for all models to determine their quality factors.

The calculated energy density spectrums for all simulated models were calculated by integrating the electromagnetic field power in cavity region for all models. Wavelength sweeps were carried out to calculate the spectrum information shown in Fig. 4-18 to Fig. 4-21. We also did Gaussian fitting on the energy density data using Matlab. The simulated wavelength sweep data obeyed Gaussian

distribution well. The black triangles were simulated data points while the red curve was the Gaussian fitting curve based on the distribution of data points. From these spectrum data, we can calculate the cavity fundamental mode resonant wavelength and quality factors by just applying Gaussian fit on them. From the definition of Gaussian distribution, we have expression

$$f(x) = \frac{1}{\sqrt{2\pi\sigma^2}} e^{\frac{-(x-a)^2}{2\sigma^2}} \tag{4.1}$$

Figure 4-18. Power density spectrums for models with $\frac{d}{a} = 0.1.$ (a) $\frac{r_1}{a} = 0.1.$ (b) $\frac{r_1}{a} = 0.15.$ (c) $\frac{r_1}{a} = 0.2.$ (d) $\frac{r_1}{a} = 0.25.$
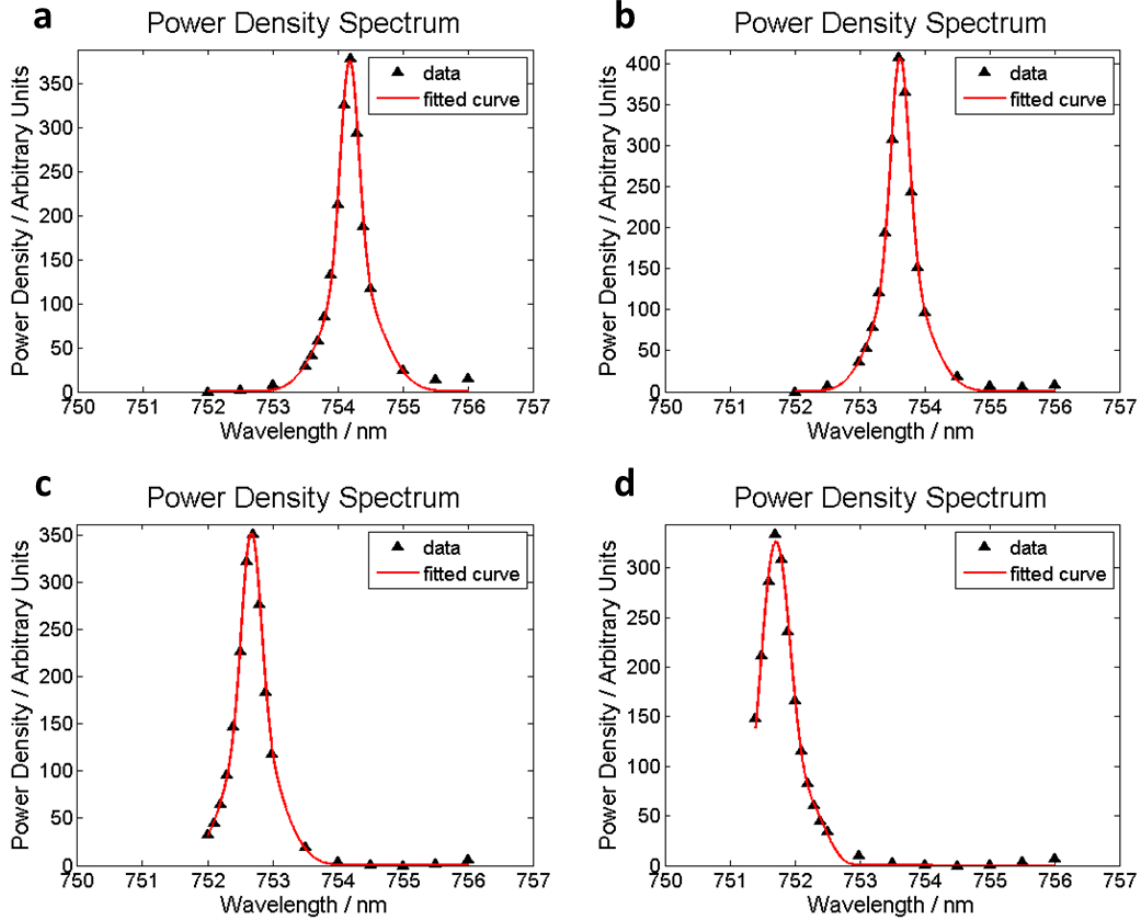
Figure 4-19. Power density spectrums for models with $\frac{d}{a} = 0.15.$ (a) $\frac{r_1}{a} = 0.1.$ (b) $\frac{r_1}{a} = 0.15.$ (c)
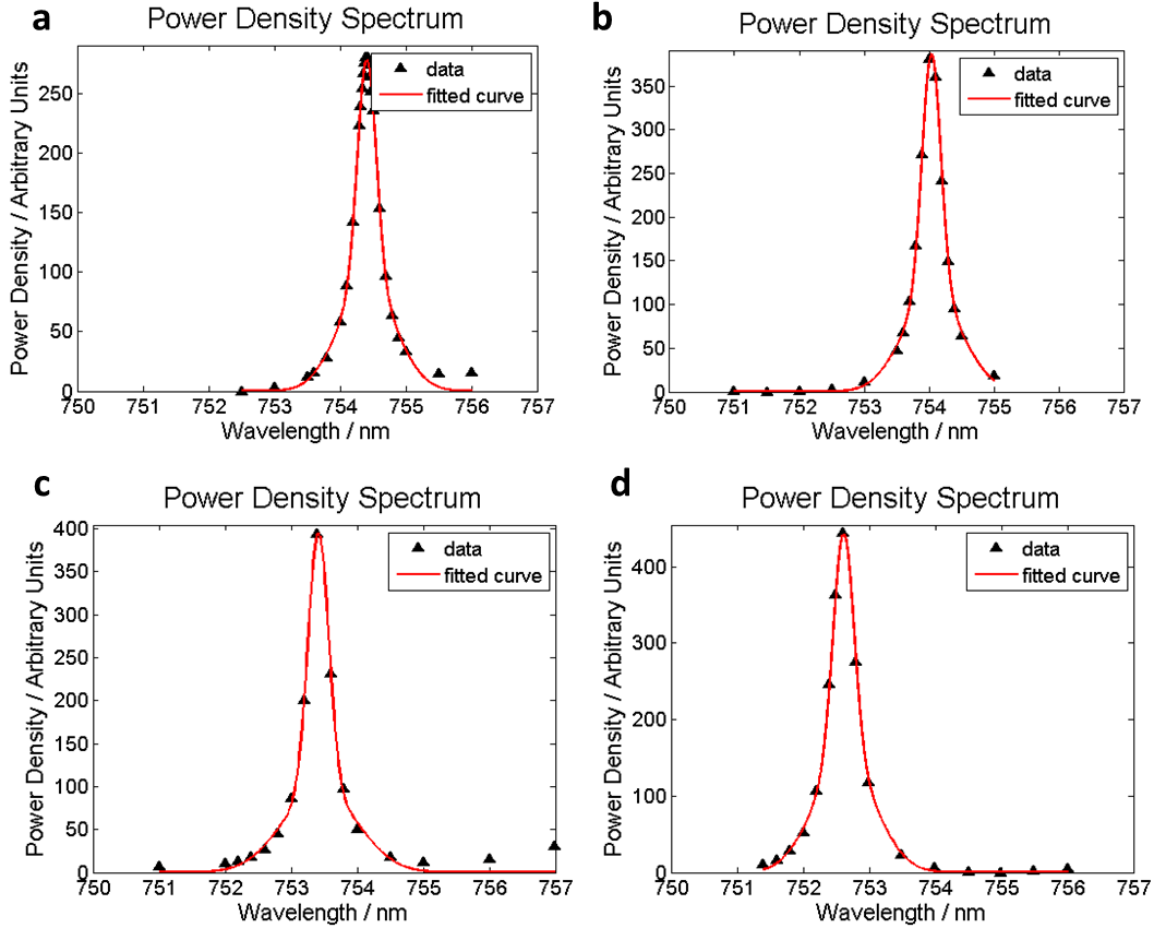
$\frac{r_1}{a} = 0.2.$ (d) $\frac{r_1}{a} = 0.25.$

Figure 4-20. Power density spectrums for models with $\frac{d}{a} = 0.2$. (a) $\frac{r_1}{a} = 0.1$. (b) $\frac{r_1}{a} = 0.15$. (c)

$\frac{r_1}{a} = 0.2$. (d) $\frac{r_1}{a} = 0.25$.
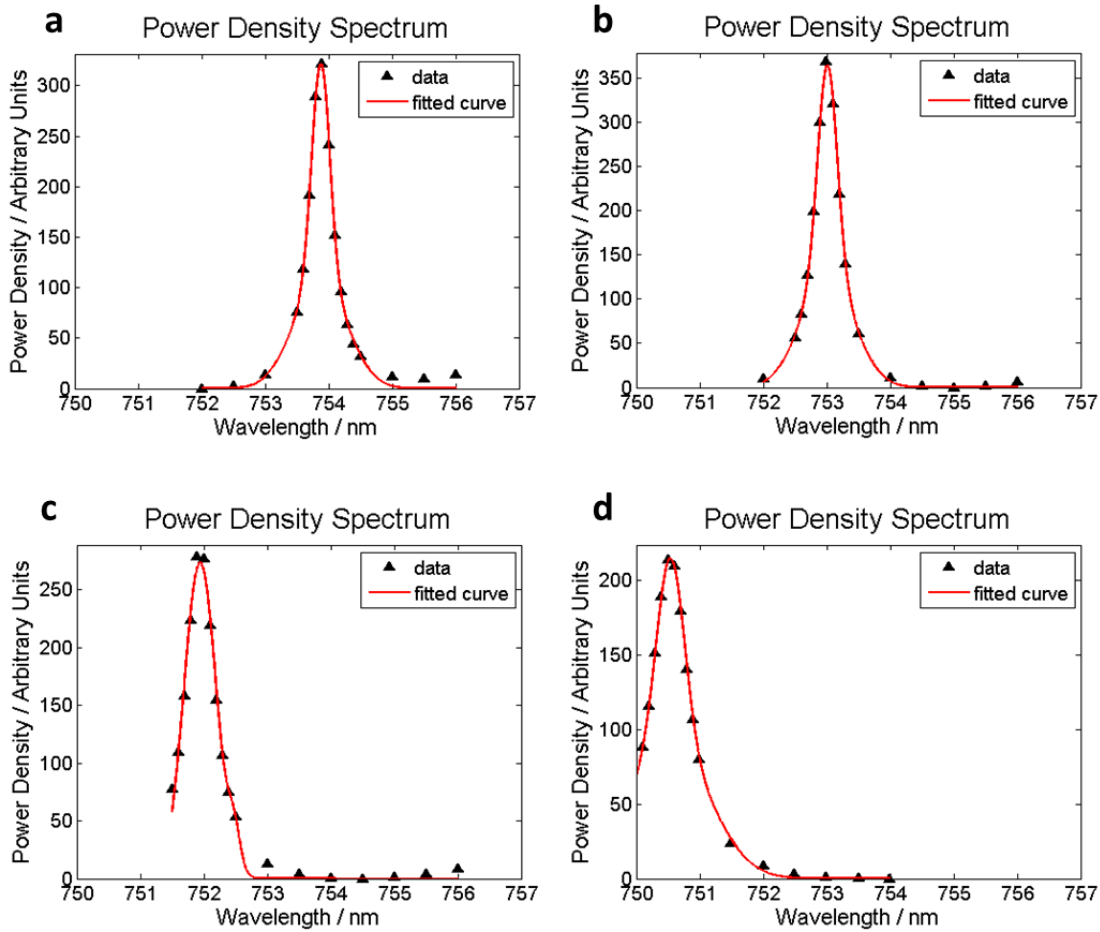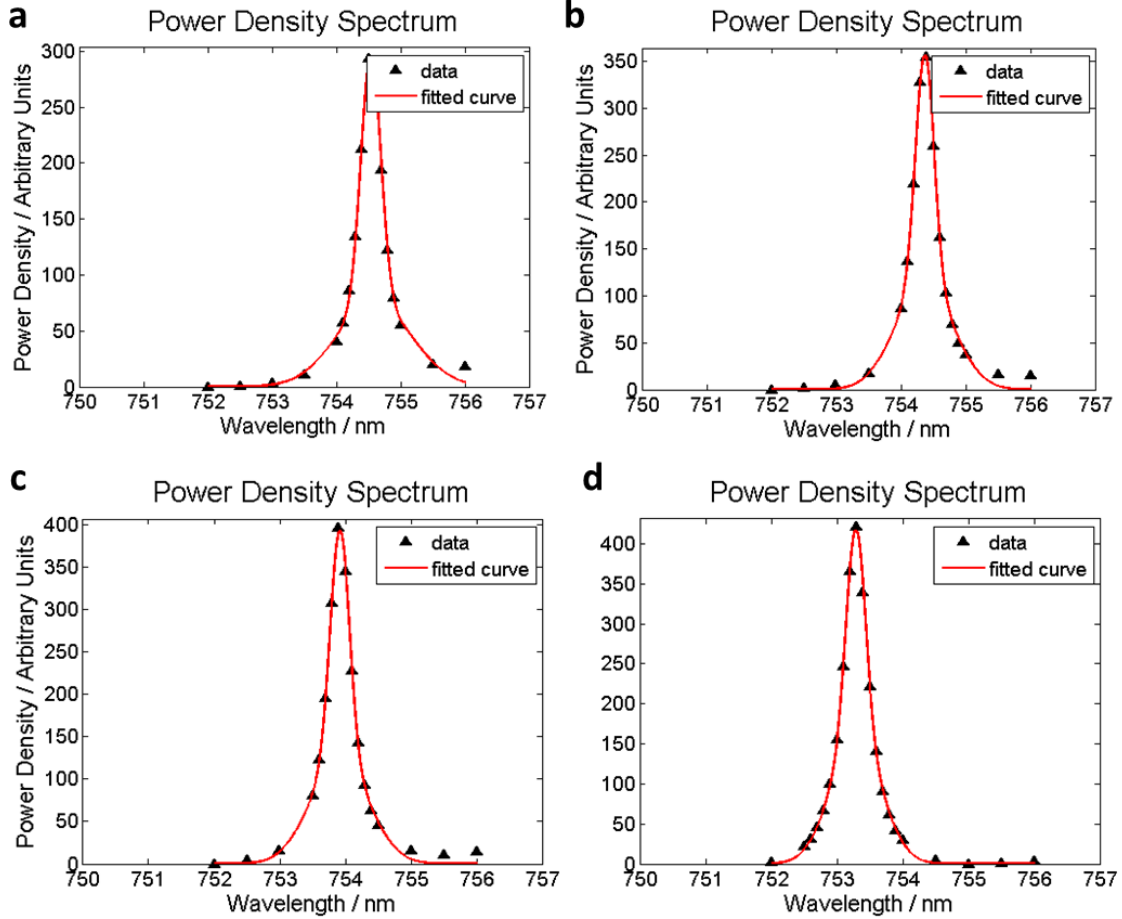
Figure 4-21. Power density spectrums for models with $\frac{d}{a} = 0.25$. (a) $\frac{r_1}{a} = 0.1$. (b) $\frac{r_1}{a} = 0.15$. (c) $\frac{r_1}{a} = 0.2$. (d) $\frac{r_1}{a} = 0.25$.

E. Cavity fundamental mode wavelength analysis

From the power density spectrums, the cavity fundamental mode wavelengths of different parameter selection sets were shown in Fig 4-22 and Table 4-1. The cavity fundamental mode resonant wavelengths of designed models fall in the range of 750 nm – 760 nm, which fulfilled our requirements.

From equation 4.3, the cavity fundamental mode wavelength can be calculated by Gaussian

fitting.
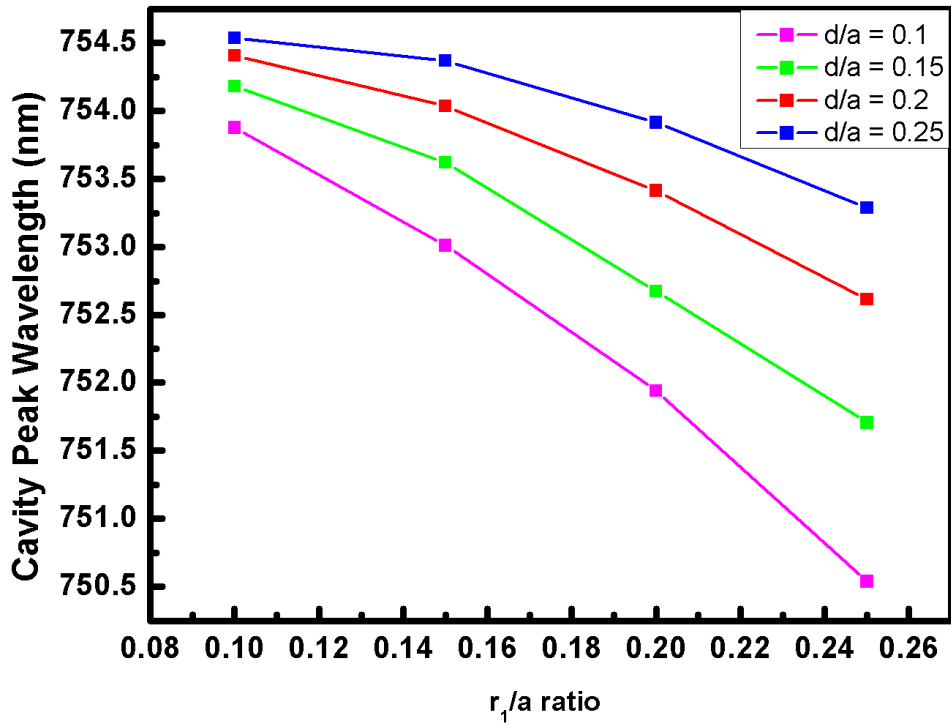
Figure 4-22. Cavity fundamental mode wavelengths of simulated models. The cavity peak wavelength decreases with increasing $\frac{r_1}{a}$ ratio and increases with increasing $\frac{d}{a}$ ratio. All modes had their cavity fundamental mode resonant wavelength in the range of 750 nm to 760 nm, which is the range of our design goal.

Table 4-1. Cavity fundamental mode resonant wavelengths of all models

$\frac{r_1}{a}$ ratio	Cavity fundamental mode resonant wavelength / nm			
	$\frac{d}{a} = 0.1$	$\frac{d}{a} = 0.15$	$\frac{d}{a} = 0.2$	$\frac{d}{a} = 0.25$
0.1	753.877018	754.182383	754.407752	754.536567
0.15	753.010636	753.621241	754.036437	754.369594
0.2	751.941448	752.672518	753.412714	753.917046
0.25	750.538297	751.706941	752.612649	753.288453

F. Cavity quality factor analysis

The quality factor is defined to characterize a resonator about its capacity to maintain its energy inside itself. Higher quality factor indicates a lower rate of energy loss relative to the stored energy thus the resonator is less damped.

The definition of the quality factor is the frequency-to-bandwidth ratio of the resonator:

$$Q = \frac{f_r}{\Delta f} \tag{4.2}$$

Where f_r is the resonant frequency, Δf is the half-power bandwidth.

We can push a little forward from the above equation:

$$Q = \frac{f_r}{\Delta f} = \frac{\frac{c}{\lambda_r}}{\frac{c}{\lambda_2} - \frac{c}{\lambda_1}} = \frac{\lambda_1 \lambda_2}{\lambda_r(\lambda_1 - \lambda_2)} \approx \frac{\lambda_r}{\Delta \lambda} \tag{4.3}$$

We further apply equation (4.1), then the cavity fundamental mode resonant wavelength and quality factor would be

$$\lambda_r = a, \ Q = \frac{a}{2\sqrt{2\ln(2)}\sigma} \tag{4.4}$$

35

From the cavity fundamental mode energy density spectrum, we can calculate the quality factors of our simulated models. The results were shown in Fig 4-23.

The results in Fig 4-23 showed the trend of the quality factor with varying $\frac{r_1}{a}$ and $\frac{d}{a}$ ratio. The quality factor increases with increasing $\frac{r_1}{a}$ and then decreases. We can pick out the model parameters with the highest model quality factor. With $\frac{r_1}{a} = 0.2$ and $\frac{d}{a} = 0.1$, the quality factor is 2563.8. The highest quality factor in our simulations is about 1.5 times of the quality factor of lowest quality factors, indicating the necessity of parameter selection and model simulation.
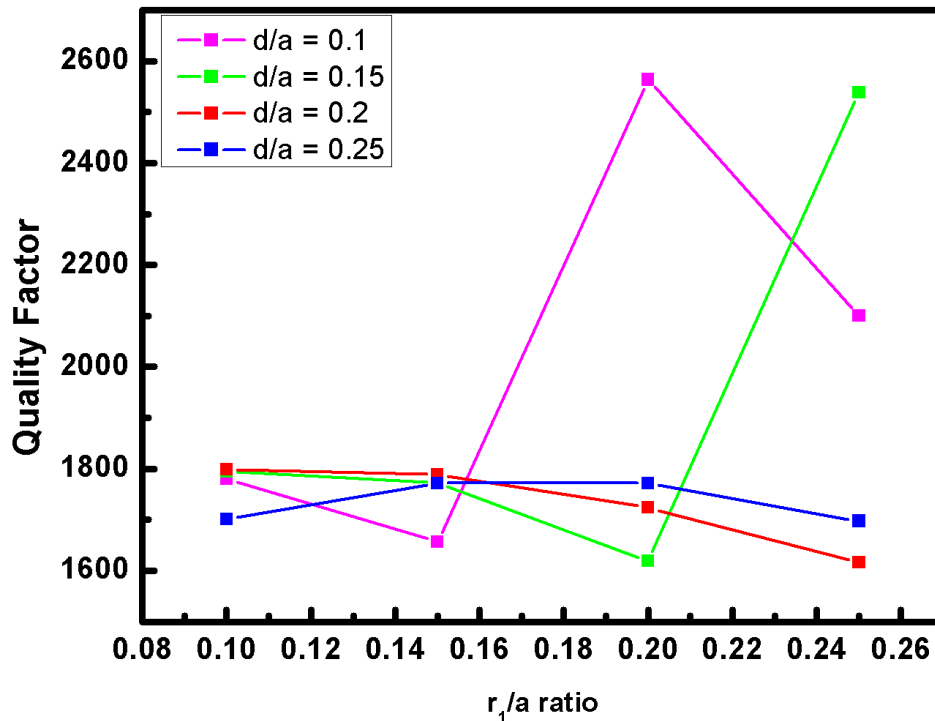
Figure 4-22. Cavity fundamental mode quality factor with respect of $\frac{r_1}{a}$ ratio and $\frac{d}{a}$ ratio. In all parameter selection sets, the parameter set with $a = 300\ nm$, $r_0 = 90\ nm$, $r_1 = 60\ nm$ and $d = 30\ nm$ has the maximum quality factor of 2563.8.

G. Summary

In this project, our goal was to design a L3 photonic crystal cavity with fundamental mode resonant wavelength in the range of 750 nm to 760 nm and with high quality factor. Our simulations on two key parameters of L3 model calculated three-dimensional electric field amplitude pattern and field energy density spectrum, from which we calculated the resonant wavelengths and quality factors through Gaussian fitting. The result indicates that the parameter selection of $a = 300\ nm$, $r_0 = 90\ nm$, $r_1 = 60\ nm$ and $d = 30\ nm$ is the optimal design. This model has its resonant wavelength of 751.94 nm and quality factor of 2563.8.

REFERENCE

1. Kneipp, K., Wang, Y., Kneipp, H., Perelman, L. T., Itzkan, I., Dasari, R. R., & Feld, M. S. (1997). Single molecule detection using surface-enhanced Raman scattering (SERS). *Physical review letters*, *78*(9), 1667.

2. Duan, X., Huang, Y., Agarwal, R., & Lieber, C. M. (2003). Single-nanowire electrically driven lasers. *Nature*, *421*(6920), 241-245.

3. Ito, Y., Matsuda, K., & Kanemitsu, Y. (2007). Mechanism of photoluminescence enhancement in single semiconductor nanocrystals on metal surfaces. *Physical review B*, *75*(3), 033309.

4. Weisbuch, C., Nishioka, M., Ishikawa, A., & Arakawa, Y. (1992). Observation of the coupled exciton-photon mode splitting in a semiconductor quantum microcavity. *Physical Review Letters*, *69*(23), 3314.

5. Nie, S., & Emory, S. R. (1997). Probing single molecules and single nanoparticles by surface-enhanced Raman scattering. *science*, *275*(5303), 1102-1106.

6. Asano, T., Song, B. S., Akahane, Y., & Noda, S. (2006). Ultrahigh-Q nanocavities in two-dimensional photonic crystal slabs. Selected Topics in Quantum Electronics, IEEE Journal of, 12(6), 1123-1134.7. Moskovits, M. (1985). Surface-enhanced spectroscopy. Reviews of modern physics, 57(3), 783.

7. Moskovits, M. (1985). Surface-enhanced spectroscopy. *Reviews of modern physics*, *57*(3), 783.

8. Qian, X., Peng, X. H., Ansari, D. O., Yin-Goen, Q., Chen, G. Z., Shin, D. M., ... & Nie, S. (2008). In vivo tumor targeting and spectroscopic detection with surface-enhanced Raman nanoparticle tags. Nature biotechnology, 26(1), 83-90.

9. Yoon, I., Kang, T., Choi, W., Kim, J., Yoo, Y., Joo, S. W., ... & Kim, B. (2008). Single nanowire on a film as an efficient SERS-active platform. Journal of the American Chemical Society, 131(2), 758-762.

10. Mekis, A., Chen, J. C., Kurland, I., Fan, S., Villeneuve, P. R., & Joannopoulos, J. D. (1996). High transmission through sharp bends in photonic crystal waveguides. Physical Review Letters, 77(18), 3787.

11. Kounoike, K., Yamaguchi, M., Fujita, M., Asano, T., Nakanishi, J., & Noda, S. (2005). Investigation of spontaneous emission from quantum dots embedded in two-dimensional photonic-crystal slab. Electronics Letters, 41(25), 1402-1403.12.

12. Yablonovitch, E. (1987). Inhibited spontaneous emission in solid-state physics and electronics. Physical review letters, 58(20), 2059.

13. Yablonovitch, E. (1987). Inhibited spontaneous emission in solid-state physics and electronics. Physical review letters, 58(20), 2059.

14. Sievenpiper, D., Zhang, L., Broas, R. F. J., Alexopolous, N. G., & Yablonovitch, E. (1999). High-impedance electromagnetic surfaces with a forbidden frequency band. Microwave Theory and Techniques, IEEE Transactions on, 47(11), 2059-2074.

15. John, S. (1987). Strong localization of photons in certain disordered dielectric superlattices. Physical review letters, 58(23), 2486.

16. John, S. (1984). Electromagnetic absorption in a disordered medium near a photon mobility edge. Physical Review Letters, 53(22), 2169.

17. Wierer, J. J., David, A., & Megens, M. M. (2009). III-nitride photonic-crystal light-emitting diodes with high extraction efficiency. Nature Photonics, 3(3), 163-169.

18. Park, H. G., Kim, S. H., Kwon, S. H., Ju, Y. G., Yang, J. K., Baek, J. H., ... & Lee, Y.

H. (2004). Electrically driven single-cell photonic crystal laser. Science, 305(5689), 1444-1447.

19. Garnett, E., & Yang, P. (2010). Light trapping in silicon nanowire solar cells. Nano letters, 10(3), 1082-1087.

20. Russell, P. (2003). Photonic crystal fibers. science, 299(5605), 358-362.

21. Maier, S. A. (2007). Plasmonics: fundamentals and applications. Springer Science & Business Media.

22. Du, Y., Yang, S., Li, H., Chen, S., & Hu, J. (2015). Particle-dressed, silica shell-isolated cavity architectures for surface-enhanced Raman scattering. Chemistry Letters, (0).

23. Liu, M., Johnston, M. B., & Snaith, H. J. (2013). Efficient planar heterojunction perovskite solar cells by vapour deposition. Nature, 501(7467), 395-398.

24. Burschka, J., Pellet, N., Moon, S. J., Humphry-Baker, R., Gao, P., Nazeeruddin, M. K., & Grätzel, M. (2013). Sequential deposition as a route to high-performance perovskite-sensitized solar cells. Nature, 499(7458), 316-319.

25. Tan, Z. K., Moghaddam, R. S., Lai, M. L., Docampo, P., Higler, R., Deschler, F., ... & Friend, R. H. (2014). Bright light-emitting diodes based on organometal halide perovskite. Nature nanotechnology.

26. Dou, L., Yang, Y. M., You, J., Hong, Z., Chang, W. H., Li, G., & Yang, Y. (2014). Solution-processed hybrid perovskite photodetectors with high detectivity. Nature communications, 5.

27. Chalcraft, A. R. A., Lam, S., O'Brien, D., Krauss, T. F., Sahin, M., Szymanski, D., ... & Hopkinson, M. (2007). Mode structure of the L3 photonic crystal cavity. Applied

Physics Letters, 90(24), 241117-241117.

28. Makarova, M., Vuckovic, J., Sanda, H., & Nishi, Y. (2006). Silicon-based photonic crystal nanocavity light emitters. Applied physics letters, 89(22), 221101.

29. Gevaux, D. G., Bennett, A. J., Stevenson, R. M., Shields, A. J., Atkinson, P., Griffiths, J., ... & Ritchie, D. A. (2006). Enhancement and suppression of spontaneous emission by temperature tuning InAs quantum dots to photonic crystal cavities. Applied physics letters, 88(13), 131101.

30. Arita, M., Ishida, S., Kako, S., Iwamoto, S., & Arakawa, Y. (2007). AlN air-bridge photonic crystal nanocavities demonstrating high quality factor. Applied Physics Letters, 91(5), 051106.

31. Meier, C., Hennessy, K., Haberer, E. D., Sharma, R., Choi, Y. S., McGroddy, K., ... & Hu, E. L. (2006). Visible resonant modes in GaN-based photonic crystal membrane cavities. Applied physics letters, 88(3), 031111.

APPENDIX I

In this appendix section, the Matlab code to calculate the positions of gold nanoparticles evenly distributed along the bowl surface of gold nano-bowl structure in chapter 2 is presented. Conjugate Gradient method is used in np_pos.m to finish this task.

```matlab
% np_pos.m version 2.0
% Sen Yang 2014/12/08
% The parts to generate other nearest gold NP from the first gold NP
% parameter definitions-------------------------------------------------
--
diameter_bowl = 620;
d1_1 = 480;
diameter_NP = 16;
distNP = 28;%distance among the gold NPs
r1 = diameter_bowl / 2 - diameter_NP / 2 ;
r2 = distNP+diameter_NP;
epsilon1 = 0.05; % The error cannot be >2 nm^2
epsilon2 = 3;
stepM = 10;% maximum step length of 10nm
SearchLabel = 1;
%----------------------------------------------------------------------
--
origin = [0 0 -sqrt((diameter_bowl/2)^2-(d1_1/2)^2)];% Center of the bowl
origin = origin';
% get the first and second points in pool
coordList = [0 0 (origin(3) - (diameter_bowl/2-diameter_NP/2))];
coordList = coordList';
%Get the second point
syms y z
[y,z] = solve('y^2+(z-origin(3))^2 == (diameter_bowl/2-
diameter_NP/2)^2','y^2+(z-coordList(3,1))^2 ==(distNP+diameter_NP)^2');
y = eval(y);
z = eval(z);
t = [0 y(1) z(1)]';
coordList = [coordList t];
Num = 2;% Total number of nanoparticle in pool
% Conjugate gradient method to calculate other gold nanoparticles in bowl
vector1 = [0 1];
point0 = coordList(:,2);
while SearchLabel == 1
    ori1 = [coordList(1,1) coordList(2,1) coordList(3,1)]';% The origin
of the first sphere space
    ori2 = [coordList(1,Num) coordList(2,Num) coordList(3,Num)]';% The
origin of the second sphere space
    vector2 = [ori2(1)-ori1(1) ori2(2)-ori1(2)];

    if vector2(1)>=0
        theta = acos(dot(vector1,vector2)/norm(vector2)) + pi/6;
        x0 = r2*sin(theta); y0 = r2*cos(theta);
    else
```

```matlab
        theta = acos(dot(vector1,vector2)/norm(vector2)) - pi/6;
        x0 = -r2*sin(theta); y0 = r2*cos(theta);
    end
    point = [ x0 y0 ori2(3)]';% The start point before searching
    label1 = 1;
    label2 = 1;
    label3 = 1;

    whileLabel = label1+label2+label3;
    % Used to get one matchpoint
    while whileLabel > 0


        %  search for point in origin spherespace
        sstep = 0.1;% step step length

        while label1 > 0

            gx = 2*(point(1) - origin(1));gy = 2*(point(2) -
origin(2));gz = 2*(point(3) - origin(3));
            g = -1*[gx gy gz]';% The gradient of first function at
present point
            g = g/norm(g);
            point1 = point;
            d1 = norm(norm(point1 - origin) - r1);% distance control
parameter
            sign = ((point(1)-origin(1))^2+(point(2)-
origin(2))^2+(point(3)-origin(3))^2-r1^2)/norm((point(1)-
origin(1))^2+(point(2)-origin(2))^2+(point(3)-origin(3))^2-r1^2);
            % To look for better step length
            i = 0;
            note = 0;
            for step1 = 0:sstep:stepM
                point1 = point + g*step1*sign;
                d2 = norm(norm(point1 - origin) - r1);
                if d2<d1
                    d1 = d2;
                    note = i;
                end
                i = i + 1;
            end
            step1 = note*sstep;
            point = point + g*step1*sign;
            if norm(norm(point - origin) - r1)>epsilon1
                label1 = 1;
            else
                label1 = 0;
            end

        end

        % search for point in second sphere space
        while label2 > 0
```

```matlab
            gx = 2*(point(1) - ori1(1));gy = 2*(point(2) - ori1(2));gz =
2*(point(3) - ori1(3));
            g = -1*[gx gy gz]';
            g = g/norm(g);% The gradient of first function at present
point
            point1 = point;
            d1 = norm(norm(point1 - ori1) - r2);% distance control
parameter
             sign = ((point(1)-ori1(1))^2+(point(2)-ori1(2))^2+(point(3)-
ori1(3))^2-r2^2)/norm((point(1)-ori1(1))^2+(point(2)-
ori1(2))^2+(point(3)-ori1(3))^2-r2^2);
            % To look for better step length
            i = 0;
            note = 0;
            for step1 = 0:sstep:stepM
                point1 = point + g*step1*sign;
                d2 = norm(norm(point1 - ori1) - r2);
                if d2<d1
                    d1 = d2;
                    note = i;
                end
                i = i + 1;
            end
            step1 = note*sstep;
            point = point + g*step1*sign;
            if norm(norm(point - ori1) - r2)>epsilon1
                label2 = 1;
            else
                label2 = 0;
            end
        end
        % search for point in third spherespace
        while label3 > 0
            gx = 2*(point(1) - ori2(1));gy = 2*(point(2) - ori2(2));gz =
2*(point(3) - ori2(3));
            g = -1*[gx gy gz]';
            g = g/norm(g);% The gradient of first function at present
point
            point1 = point;
            d1 = norm(norm(point1 - ori2) - r2);% distance control
parameter
            sign = ((point(1)-ori2(1))^2+(point(2)-ori2(2))^2+(point(3)-
ori2(3))^2-r2^2)/norm((point(1)-ori2(1))^2+(point(2)-
ori2(2))^2+(point(3)-ori2(3))^2-r2^2);
            % To look for better step length
            i = 0;
            note = 0;
            for step1 = 0:sstep:stepM
                point1 = point + g*step1*sign;
                d2 = norm(norm(point1 - ori2) - r2);
                if d2<d1
                    d1 = d2;
                    note = i;
                end
                i = i + 1;
```

```matlab
                end
                step1 = note*sstep;
                point = point + g*step1*sign;
                if norm(norm(point - ori2) - r2)>epsilon1
                    label3 = 1;
                else
                    label3 = 0;
                end
            end
            if norm(norm(point - origin) - r1) > epsilon1
                label1 = 1;
            else
                label1 = 0;
            end
            if norm(norm(point - ori1) - r2) > epsilon1
                label2 = 1;
            else
                label2 = 0;
            end
            if norm(norm(point - ori2) - r2) > epsilon1
                label3 = 1;
            else
                label3 = 0;
            end
            whileLabel = label1+label2+label3;

        end
        if norm(point - point0) >= r2/2
            coordList = [coordList point]; % add one point into the pool
            Num = Num + 1;
            SearchLabel = 1;
        else
            SearchLabel = 0;
        end
    end
coordList = coordList * 1e-9;
```

APPENDIX II

In this section, the Matlab code for Gaussian lineshape fitting in chapter 4 is presented.

This code also calculates the quality factor from spectrum and write them in text files.

```matlab
%Gaussian_fit.m
%Sen Yang 2015/09/21
%This file is used to fit the power density spectrums of PCC from
%simulations.
allFiles = dir('.');
allnames = {allFiles(arrayfun(@(x) ~x.isdir, allFiles)).name};
numOfFiles = size(allnames);
numOfFiles = numOfFiles(:, 2);
iter = 1; % first is . and second is ..
while iter < numOfFiles - 1
    curName = char(allnames(iter));
    fileID = fopen(curName, 'r');
    A = fscanf(fileID, '%f');
    tot = size(A);
    row = tot(:, 1);
    x = [];
    y = [];
    for i = 2 : 2 : row
        x = [x A(i - 1)];
        y = [y, A(i)];
    end
    y = y - min(y);
    ymax = max(y) / 2;
    f = fit(x', y','gauss2');
    %plot of data points and fit curve
    fig = figure(iter);
    p = plot(f, x, y, '^');
    set(p(1), 'MarkerEdgeColor', 'k', 'MarkerFaceColor', 'k');
    set(p, 'LineWidth', 2);
    set(gca, 'FontSize', 14);
    title('Power Density Spectrum', 'FontName', 'Arial', 'FontSize', 20);
    xlabel('Wavelength / nm', 'FontName', 'Arial', 'FontSize', 16);
    ylabel('Power Density / Arbitrary Units','FontName', 'Arial',
'FontSize', 16);
    axis([750 757 0 max(y) + 10]);
    %plot ended
    % write a binary-find
    index11 = 752;
    index12 = f.b1;
    index21 = f.b1;
    index22 = 756;
    step = 1e-3;
    while(index12 - index11 > step)
        mid = (index11 + index12) / 2;
        if(f(mid) > ymax)
            index12 = mid;
        else
```

```matlab
            index11 = mid;
        end
    end

    while(index22 - index21 > step)
        mid = (index21 + index22) / 2;
        if(f(mid) > ymax)
            index21 = mid;
        else
            index22 = mid;
        end
    end
    Qfactor = f.b1 / (index22 - index12);
    fclose(fileID);
    fileID = fopen(curName, 'w');
    formatSpec = 'Quality factor is %f, peak wl is %f';
    fprintf(fileID, formatSpec, Qfactor, f.b1);
    fclose(fileID);
    iter = iter + 1;
end
```